MNRAS 000, 1–13 (2018) Preprint 22 March 2022 Compiled using MNRAS LATEX style file v3.0

The Main Sequence of star forming galaxies across cosmic times

P. Popesso,[1]★ A. Concas,[1] G. Cresci,[2] S. Belli,[3] G. Rodighiero,[4] H. Inami,[5] M. Dickinson,[6] O. Ilbert,[7] M. Pannella,[8] D. Elbaz,[9]

[1]European Southern Observatory, Karl Schwarzschildstrasse 2, 85748, Garching bei München, Germany
[2]INAF-Osservatorio Astronomico di Arcetri, Largo Enrico Fermi 5, 50125, Firenze, Italy
[3]Center for Astrophysics Harvard & Smithsonian, 60 Garden St., Cambridge, MA 02138
[4]Dipartimento di Fisica e Astronomia, Universitá di Padova, Vicolo dell' Osservatorio 3, 35122, Padova, Italy
[5]Hiroshima Astrophysical Science Center, 1-3-2 Kagamiyama, Higashi-Hiroshima City, Hiroshima, Japan 739-8511
[6]NOIRLab, 950 N. Cherry Ave. Tucson, AZ 85719, USA
[7]Laboratoire d'Astrophysique de Marseille, 38 rue Frederic Joliot Curie, 13388 Marseille, France
[8]Dipartimento di Fisica e Astronomia, Universitá di Trieste, Via Valerio, 2 - 34127 Trieste, Italy
[9]Laboratoire AIM-Paris-Saclay, CEA/DRF/Irfu - CNRS - Université Paris Diderot, CEA-Saclay, 91191 Gif-sur-Yvette, France

Accepted XXX. Received YYY; in original form ZZZ

ABSTRACT

By compiling a comprehensive census of literature studies, we investigate the evolution of the Main Sequence (MS) of star forming galaxies (SFGs) in the widest range of redshift ($0 < z < 6$) and stellar mass ($10^{8.5} - 10^{11.5}\ M_{\odot}$) ever probed. We convert all observations to a common calibration and find a remarkable consensus on the variation of the MS shape and normalization across cosmic time. The relation exhibits a curvature towards the high stellar masses at all redshifts. The best functional form is governed by two parameters: the evolution of the normalization and the turn-over mass ($M_0(t)$), which both evolve as a power law of the Universe age. The turn-over mass determines the MS shape. It marginally evolves with time, making the MS slightly steeper towards $z \sim 4-6$. At stellar masses below $M_0(t)$, SFGs have a constant specific SFR (sSFR), while above $M_0(t)$ the sSFR is suppressed. We find that the MS is dominated by central galaxies. This allows transforming $M_0(t)$ into the corresponding host halo mass. This evolves as the halo mass threshold between cold and hot accretion regimes, as predicted by the theory of accretion, where the central galaxy is fed or starved of cold gas supply, respectively. We, thus, argue that the progressive MS bending as a function of the Universe age is caused by the lower availability of cold gas in halos entering the hot accretion phase, in addition to black hole feedback. We also find qualitatively the same trend in the largest sample of star forming galaxies provided by the IllustrisTNG simulation, although we note still large discrepancy with respect to observations.

Key words: galaxies: evolution – galaxies: star formation – galaxies: high-redshift

1 INTRODUCTION

The Main Sequence (MS) of star forming galaxies (SFGs) is considered one of the most useful tools in modern astrophysics in the field of galaxy evolution. This very tight relation between the galaxy star formation rate (SFR) and the stellar mass ($M_\star$) is in place from redshift ~ 0 up to ~ 6 (Brinchmann et al. 2004; Salim et al. 2007; Noeske et al. 2007; Elbaz et al. 2007; Daddi et al. 2007; Chen et al. 2009; Pannella et al. 2009; Santini et al. 2009; Oliver et al. 2010; Magdis et al. 2010; Rodighiero et al. 2011; Elbaz et al. 2011; Karim et al. 2011; Shim et al. 2011; Whitaker et al. 2012; Zahid et al. 2012; Lee et al. 2012; Reddy et al. 2012; Salmi et al. 2012; Moustakas et al. 2013; Kashino et al. 2013; Sobral et al. 2014; Steinhardt et al. 2014; Speagle et al. 2014; Whitaker et al. 2014; Shivaei et al. 2015; Schreiber et al. 2015; Tasca et al. 2015; Lee et al. 2015; Kurczynski et al. 2016; Erfanianfar et al. 2016; Santini et al. 2017; Pearson et al. 2018; Belfiore et al. 2018; Popesso et al. 2019a,b; Leslie et al. 2020). The evolution of its normalization, slope and scatter have been largely studied in the past decade. It is now well established that the normalization declines significantly but smoothly as a function of redshift, likely on mass-dependent timescales (see also Speagle et al. 2014), rather than being driven by stochastic events like major mergers and starbursts (Oemler et al. 2017). More uncertain is the precise redshift dependence of such evolution, which is often expressed as $\propto (1+z)^{\gamma}$, with γ varying from 1.9 to 3.7 (Speagle et al. 2014; Whitaker et al. 2014; Schreiber et al. 2015; Ilbert et al. 2013; Pearson et al. 2018). This is mainly due to the uncertainty in deriving the evolution of the exact shape of the relation, which is still matter of intense debate. Several studies point to a power law shape, SFR $\propto M_\star^{\alpha}$, with an intrinsic scatter of

★ E-mail: paola.popesso@eso.de

about 0.2-0.3 dex for moderate to relatively low stellar mass galaxies, both in the local Universe (Peng et al. 2010; Renzini & Peng 2015) and at high redshift (Speagle et al. 2014; Rodighiero et al. 2014; Kurczynski et al. 2016; Pearson et al. 2018). Other works suggest that the relation exhibits a curvature towards the high mass at low (Popesso et al. 2019b) and high redshift (Whitaker et al. 2014; Schreiber et al. 2015; Lee et al. 2015; Tasca et al. 2015; Tomczak et al. 2016; Popesso et al. 2019a).

Most of this discrepancy is ascribable to how SFGs are selected in first place, on the SFR estimators and on the method of localization of the MS. Popesso et al. (2019a) show that color-color selection of SFGs lead to the exclusion of red dusty star forming galaxies in particular at $z > 1.5$ and to a steep MS. Tomczak et al. (2016) show that without any selection, the MS is bending more significantly in the local than in the distant Universe. The magnitude of these effects precludes robust interpretations of derived MS properties. To overcome this problem, and so constrain the MS evolution and systematic errors, Speagle et al. (2014, hereafter S14) have compiled 64 MS observations from 25 studies published in the period 2007-2014, spanning $z \sim 0-6$, and converted them to the same absolute calibration. These MS estimates have been taken from a variety of fields, selected using different methodologies, including both stacked and non-stacked data, and estimated with a variety of SFR indicators. By calibrating consistently all datasets, S14 determine the MS best fit as a power law, with a slope marginally evolving with redshift.

Lutz (2014) nicely show that far-infrared (FIR) and ultraviolet (UV) emissions are the two key components for accurately measuring the SFR of an object. Part of the UV emission originated from the young star population is absorbed by dust and re-processed at infrared wavelengths. Such emission alone can provide a measure of the SFR only if corrected for this absorption. However, the measure of the dust attenuation is still uncertain because of the degeneracies between age and reddening, the assumption on galaxy metallicity and SF histories and the parametrization of the extinction curve (e.g. Meurer et al. 1999; Dale et al. 2009; Dunlop et al. 2017; Bourne et al. 2017). As a result, the combination of far-IR and UV emission is considered the most accurate way to determine the galaxy SFR (see Lutz 2014, and references therein). The combination of mid-infrared and UV emission can serve as well as SFR estimator. However, the contamination by AGN and the overestimation of the SFR for starburts galaxies make of the mid-infrared emission, based e.g. on *Spitzer* MIPS 24 μm data, a less accurate indicator (Elbaz et al. 2011; Nordon et al. 2010). It is worth noticing that of the 25 papers considered in S14, only two are based on the most recent far-infrared *Herschel* data (Elbaz et al. 2011; Oliver et al. 2010). The remaining 23 publications are based on Hα in emission and absorption, dust corrected far-UV and UV emission, radio data, *Spitzer* MIPS 24μm data and the combination of UV and mid-infrared data. It is not surprising, then, that S14 find out a quite large inter-publication scatter on the MS locations, which leads to a large uncertainty of their final best fit, despite the consistent calibration.

In this paper, we adopt the same approach of S14, but extend the collection of MS determination of S14 to the most recent estimates of the MS based on the combination of *Herschel* far-infrared data and UV emission in the period after 2014. These include additional 20 MS publications, for a total of 78 MS measurements at $0 < z < 6$, that we convert to the same IMF and calibrate in a consistent framework. We collect a sample of about 700 consistently calibrated data-points that express the location of the MS as a function of stellar mass and time, to estimate the evolution of the MS across cosmic time and how this drives the star formation rate density of our Universe.

The paper is structured as follows. Section 1 describes the MS compilation. Section 2 presents our best-fitting procedure. Section 3 shows our results. Section 4 provides a summary of our findings. We assume a ΛCDM cosmology with $\Omega_M = 0.3$, $\Omega_\Lambda = 0.7$ and $H_0 = 70$ *km/s/Mpc*, and a Kroupa IMF throughout the paper.

2 THE MS COLLECTION

In this work, we focus on MS estimates that have been published after 2014. To consider in the analysis the MS measurements that have been published in the period 2007-2014, we include here the MS relation determined by S14 as a result of a compilation of 64 MS estimates collected in 25 papers (see Table 3 of S14). We consider, in particular, the fit n. 64, which S14 provide as their reference MS. To this, we add all the MS relations that satisfy the following criteria:

(i) Includes a published $M_\star - SFR$ or $M_\star - sSFR$ (sSFR=SFR/$M_\star$) relation (slope α and normalization β) or otherwise analogous quantities;
(ii) Fit(s) includes more than two data points (if stacked) or 50 galaxies (if directly observed). This is required to avoid biases resulting from small number statistics;
(iii) Stacked points must provide mean or median of more than 25 points, to avoid large uncertainties due to low number statistics;
(iv) Published after 2014.

The 21 publications that are retrieved considering these criteria are listed in Table 1, together with the used IMF, SFR indicator, redshift range, cosmological parameters, SFGs selection method, and extinction curve. In Appendix, we provide a full description of the individual publication data.

All the considered MS estimates are based on the deepest UV, optical, IR and radio surveys ever realized on the CANDELS, COSMOS and ECDFS fields at intermediate and high redshift, and on the WISE, GALEX and optical spectroscopy in the SDSS area at $z \sim 0$. Of these, 10 publications (Heinis et al. 2014; Whitaker et al. 2014; Chang et al. 2015; Lee et al. 2015; Ilbert et al. 2015; Schreiber et al. 2015; Tomczak et al. 2016; Pearson et al. 2018; Lee et al. 2018; Popesso et al. 2019a) out of 20 are based on a SFR indicator given by the combination of UV and IR data. Additional 3 are based only on far-infrared PACS data (Rodighiero et al. 2014; Erfanianfar et al. 2016; Popesso et al. 2019a). Other 2 (Renzini & Peng 2015; Belfiore et al. 2018) are based on $H\alpha$ derived SFR taken from the SDSS spectroscopic dataset (Brinchmann et al. 2004). Of the remaining, 3 include SFR derived through SED fitting technique (Tasca et al. 2015; Santini et al. 2017; Kurczynski et al. 2016), one is based on the evolution of the galaxy stellar mass function of star forming galaxies (Davidzon et al. 2018), one is based on deep radio data (Leslie et al. 2020), and S14 is based on a collection of different SFR estimators. According to the definition of S14, all of the considered publications but two are based on "mixed" methods (see next section) for the selection of SFGs. These include color-color techniques (BzK, UVJ and NUVRJ), 2σ clipping, and bimodality in the SFR-$M_\star$ plane. Only 2 publications have a MS obtained for blue and active galaxies selected in the UV or with the Lymann Break Galaxy (LBG) technique.

Differently from S14, we include in our study also the MS estimate at $z \sim 0$. S14 discuss the inability to distinguish a "best" MS fit among the available $z \sim 0$ estimates obtained before 2014.

Table 1. Col. 1: Reference. Col. 2: Assumed stellar initial mass function. Col. 3: Star formation rate indicator. Col. 4: redshift range analysed Col. 5: Assumed cosmology. Col. 6: Selection methods used for the parent samples (see Appendix or individual papers for more details). Col. 7: type of data retrieved in the paper: *stacked* stands for stacked SFR data-points as a function of stellar mass and redshift, *data-points* for average or median SFR data-points as a function of stellar mass and redshift, and *best fit* stands for best-fit parameters expressing the MS shape as a function of stellar mass over the retrieved stellar mass and redshift ranges. Col. 8: Extinction curve reference: the details of the extinction curve implemented in MAGPHYS can be found in da Cunha et al. (2008), C00 refers to Calzetti et al. (2000), CF00 to Charlot & Fall (2000). Col 9: indicates whether the data have been included in (✓symbol) or excluded from (− symbol) the current analysis. The reasons for excluding an individual dataset from the analysis are given in Section 2.

Paper	IMF	SFR indicator	z range	$(h, \Omega_m, \Omega_\Lambda)$	Selection	data type	Extinction curve	included
Speagle et al. (2014)	K	mixed	0.2 – 6	0.7, 0.3, 0.7	mixed	best fit	NA	✓
Rodighiero et al. (2014)	S	IR	1.4 – 2.5	0.7, 0.25, 0.75	BzK	stacked	NA	✓
Heinis et al. (2014)	C	SED+IR	1.5 – 4	0.7, 0.3, 0.7	UV	stacked	NA	✓
Whitaker et al. (2014)	C	NUV+IR	0.5 – 2.5	0.7, 0.3, 0.7	UVJ	stacked	NA	✓
Chang et al. (2015)	C	SED+IR	< 0.1	0.7, 0.3, 0.7	mixed	best fit	MAGPHYS	–
Lee et al. (2015)	C	NUV+IR	0.3 – 1.3	0.7, 0.28, 0.72	NUVRJ	stacked	NA	✓
Ilbert et al. (2015)	C	NUV+IR	0.2 – 1.4	0.7, 0.3, 0.7	NUVRJ	data-points	NA	✓
Tasca et al. (2015)	C	SED	0.4 – 5	0.7, 0.3, 0.7	LBG+I_{AB} < 25	data-points	C00	✓
Renzini & Peng (2015)	C	Hα	< 0.085	0.7, 0.3, 0.7	mixed	best fit	CF00	✓
Schreiber et al. (2015)	S	FUV+IR	0.3 – 4	0.7, 0.3, 0.7	UVJ	stacked	NA	✓
Erfanianfar et al. (2016)	C	IR	0.2 – 1.5	0.7, 0.3, 0.7	mixed	data-points	NA	✓
Tomczak et al. (2016)	C	NUV+IR	0.2 – 3	0.7, 0.3, 0.7	UVJ	stacked	NA	✓
Santini et al. (2017)	S	SED	1.3 – 6	0.7, 0.3, 0.7	(4)	best fit	C00	✓
Kurczynski et al. (2016)	S	SED	0.5 – 3	0.7, 0.3, 0.7	UVJ	best fit	C00	✓
Pearson et al. (2018)	C	SED+IR	0.2 – 6	0.704, 0.272, 0.728	UVJ	best fit	CF00	✓
Belfiore et al. (2018)	C	Hα	< 0.1	0.7, 0.3, 0.7	mixed	best fit	CF00	✓
Davidzon et al. (2018)	C	GSMF	2 – 6	0.7, 0.3, 0.7	NUVRJ	stacked	C00	✓
Lee et al. (2018)	C	FUV+IR	1.2 – 4	0.7, 0.3, 0.7	UVJ	stacked	NA	✓
Popesso et al. (2019a)	C	IR/Hα	< 0.085	0.7, 0.3, 0.7	mixed	data-points	NA	✓
Popesso et al. (2019b)	C	FUV+IR	0.2 – −2.5	0.7, 0.3, 0.7	mixed	data-points	NA	✓
Leslie et al. (2020)	C	radio	0.3 – −5	0.7, 0.3, 0.7	NUVRJ	stacked	NA	✓

Thus, they decide not to include at all the local MS estimates. Popesso et al. (2019b) discuss extensively all the datasets available in the local Universe, selection effects and different SFR estimators and the level of agreement between the different estimates. On the basis of these results, we conclude that the inter-publication scatter of the local MS estimates available in the period 2014-2022 is comparable to that found at higher redshifts. Indeed, no different level of agreement is found as a function of redshift, once all MS estimates are brought to the same calibration (see next section for more details).

From each publication either we take the mean or median SFR data-points or staked SFR data-points at the observed stellar mass and redshift without any extrapolation or interpolation, or, if these are not available, we use the provided MS best fit parameters at a given redshift to estimate the MS in the provided stellar mass range in bins of 0.15 dex in stellar mass. The bin width is chosen to be representative of the average stellar mass error of the considered papers. The mass ranges have either been taken directly from the paper in question or estimated based on the data included in the relevant fits, rounded to the nearest 0.1 dex (see Appendix for a detailed description of the data taken from each publication). This leads to 85 determinations of the MS for a sample of ∼ 750 data-points of MS SFR as a function of stellar mass and redshift or time ($SFR(M_*, z)$ or $SFR(M_*, t)$). The data collected here encompass the widest range in redshift ($0 < z < 6$), stellar mass ($10^{8.5} - 10^{11.5}$ $M_\odot$) and SFR ($0.01 - 500$ $M_\odot \mathrm{yr}^{-1}$) available in the literature, and intend to give a census of most of the techniques and methods used to derived the MS location. Following the example of S14, we present what we hope is the broadest and most accurate census of MS observations to date.

2.1 MS calibration

As underlined in S14, several aspects need to be taken care of when comparing different MS estimates and before attempting any analysis:

(i) Initial Mass Function;
(ii) SFR estimator;
(iii) SPS model;
(iv) cosmology;
(v) emission line effect in the estimate of SFR and $M_\star$;
(vi) Star formation histories (SFH);
(vii) dust extinction curve;
(viii) photo-z biases;
(ix) SED fitting procedures;
(x) selection effects due to different SFG population selection.

A detailed discussion in S14 points out that only the points *i)*, *ii)* and *iii)* lead to relevant corrections when calibrating all the MS estimates to a common ground. Instead, different cosmologies (*iv*) have relatively negligible effects (< 0.05 dex) at $0 < z < 6$, which is the same redshift range considered here. The effect of emission lines (*v*) in the estimate of $M_\star$ and SFR is relevant only when the multi-wavelength information are limited to few photometric bands. They are, instead, negligible for datasets like CANDELS, and COSMOS, as those considered here. Following the approach of S14, we choose not to adjust our results for differences in assumed

star formation history (*vi*), dust attenuation curves (*vii*), possible photo-z biases (*viii*), or differences in SED fitting procedures (*ix*). As discussed in S14, these aspects together might lead to a correction, but there is no way to estimate their precise effect on SFR and $M_\star$ estimates. Instead, SFG selection methods (*x*) can lead to substantially different MS slopes. S14 distinguish between "bluer", "mixed", and "non-selective" techniques: "bluer" methods are based on a simple color cut to select blue galaxies, "mixed" ones involve a more sophisticated distinction between star forming and quiescent galaxies, while "non-selective" ones do not apply any selection. In particular, S14 find that "bluer"-based ("non-selective"-based) MS slopes are biased towards values closer to unity (zero), with respect to "mixed"-based slopes.

To bring every relation onto a common framework, we apply the following steps. We use the the Equations reported in Section 2.2 to convert the $M_\star$ values to a Kroupa IMF, and the SFR estimates to the Kennicutt & Evans (2012, hereafter KE12) calibration (based on the Kroupa IMF). We adjust for differences in cosmology using the $(h, \Omega_M, \Omega_\Lambda) = (0.7, 0.3, 0.7)$ WMAP concordance cosmology (Spergel et al. 2003). As the MS estimates considered in this work are all based on Bruzual & Charlot (2003) SPS model, no correction is needed. Furthermore, no additional dust correction is required, as dust has been corrected for in the considered publications, and different extinction curves do not have significant impact on the MS determination (see S14). Finally, as only 2 (Tasca et al. 2015; Heinis et al. 2014) out of the 20 MS estimates considered here are consistent with a "bluer" selection, we do not correct in this respect, but we discuss possible biases on the result.

As pointed out in Popesso et al. (2019b), another source of small discrepancy among different MS estimates is the method used to determine the MS location, e.g. as the mean or median SFR of the SFG population in the MS region. A correction can be made in this respect under the assumption that the SFR distribution at fixed $M_\star$ is log-normal in the MS region. This assumption is justified by several works in literature, which find a log-normal distribution with a rather constant dispersion of ~ 0.3 dex at any stellar mass (Daddi et al. 2007; Rodighiero et al. 2011; Schreiber et al. 2015; Popesso et al. 2019b,a). In this case, the peak of the distribution coincides with the median SFR. The mean SFR is always larger than the median by an offset that depends only on the dispersion of the distribution. For a dispersion of ~ 0.3 dex, the correction is ~ 0.1 dex. In the further analysis we apply such correction to all MS estimates based on the median SFR to convert them in mean values.

2.2 The main corrections

We describe here the corrections applied to bring the different MS estimates to a common framework:

- **IMF correction**

We apply the IMF offsets to stellar masses as in S14 with the form:

$$M_{\star,K} = 1.06\, M_{\star,C} = 0.62\, M_{\star,S}, \quad (1)$$

with the subscripts referring to Kroupa, Chabrier, and Salpeter IMFs, respectively. These correspond to stellar mass offsets of 0.03 and -0.21 dex, for the Chabrier and the Salpeter IMF, respectively.

- **SFR indicator correction**

All SFR estimates have been converted to the calibration of KE12, which is based on the Kroupa IMF. The KE12 prescriptions are different depending on whether νL_ν is estimated in the FUV ($\sim$1300–1700Å) or NUV ($\sim$2300–2800Å). Following Tables 1 and 2 of KE12, we make use of the following calibrations:

$$SFR(FUV + IR) = 1.71 \cdot 10^{-10}(L_{FUV} + 0.46 * L_{IR}) \quad (2)$$

$$SFR(NUV + IR) = 2.06 \cdot 10^{-10}(L_{NUV} + 0.27 * L_{IR}) \quad (3)$$

$$SFR(H\alpha) = 2.06 \cdot 10^{-8}(L_{H\alpha}) \quad (4)$$

$$SFR(IR) = 1.49 \cdot 10^{-10}(L_{IR}) \quad (5)$$

$$SFR(1.4GHz) = 2.43 \cdot 10^{5}(L_{1.4GHz}) \quad (6)$$

where L_{IR}, L_{FUV}, L_{NUV} and $L_{H\alpha}$ are the luminosities (in solar luminosity units) estimated in the IR (range $8-1000\,\mu$m), FUV and NUV, $H\alpha$ emission line and radio emission (140 GHz), respectively. The SFRs based on SED modelling, instead, are corrected only for the IMF, according to the derivative of Eq. 1. The correction to a common SFR indicator varies from 0.05 to -0.2 dex. After applying the calibration, the local MS of Chang et al. (2015) is still systematically lower with respect to the other local MS estimates by 0.15 dex (see Popesso et al. 2019b for a detailed comparison with UV+IR based and Hα based SFR). Thus, we correct for this offset as indicated in Popesso et al. (2019b) before including the MS estimate of Chang et al. (2015) into our sample.

As already pointed out in Popesso et al. (2019b), Pearson et al. (2018) report a systematic offset of their SFR of $\sim$0.4 dex below all other SFR estimates considered here at the same redshift. As shown in Popesso et al. (2019b), their MS lies below all other determinations at more than 1σ at all redshift. Elbaz et al. (2011) show that SPIRE and PACS SFR estimators lead to consistent results. So we conclude that the discrepancy must be related to the deblending technique of the SPIRE detections and the SED fitting technique applied in Pearson et al. (2018, see their Appendix C for an extensive discussion). Since the problem might be related to an over-blending issue rather than to the SFR indicator, we decide not to correct the SFR of Pearson et al. (2018) and to exclude those MS estimates from the dataset. Thus, the final sample of publications include 18 of the results listed in Table 1.

- **Cosmology correction**: this is calculated as the ratios between luminosity distance, $d_L(z)$, derived from two different cosmologies, and, given the observed redshift range of a sample, applying a d_L^2 correction at the expected median z of galaxies in the sample. S14 estimate also first-order volume effects. However, they find that this account for a negligible effect in all cases. Thus, we do not take it into account.

After applying the calibration, we obtain an inter-publication scatter of 0.07 dex per bin of time and stellar mass.

2.3 Selection effects

While efficient at selecting SFGs, most selection techniques differ from each other and do not all select the same population. S14 discuss extensively that the selection of blue objects preferentially select actively star-forming, non-dusty galaxies and exclude a large percentage of galaxies that are classified as SFGs via other selection mechanisms (e.g. color-color selection). This leads on average

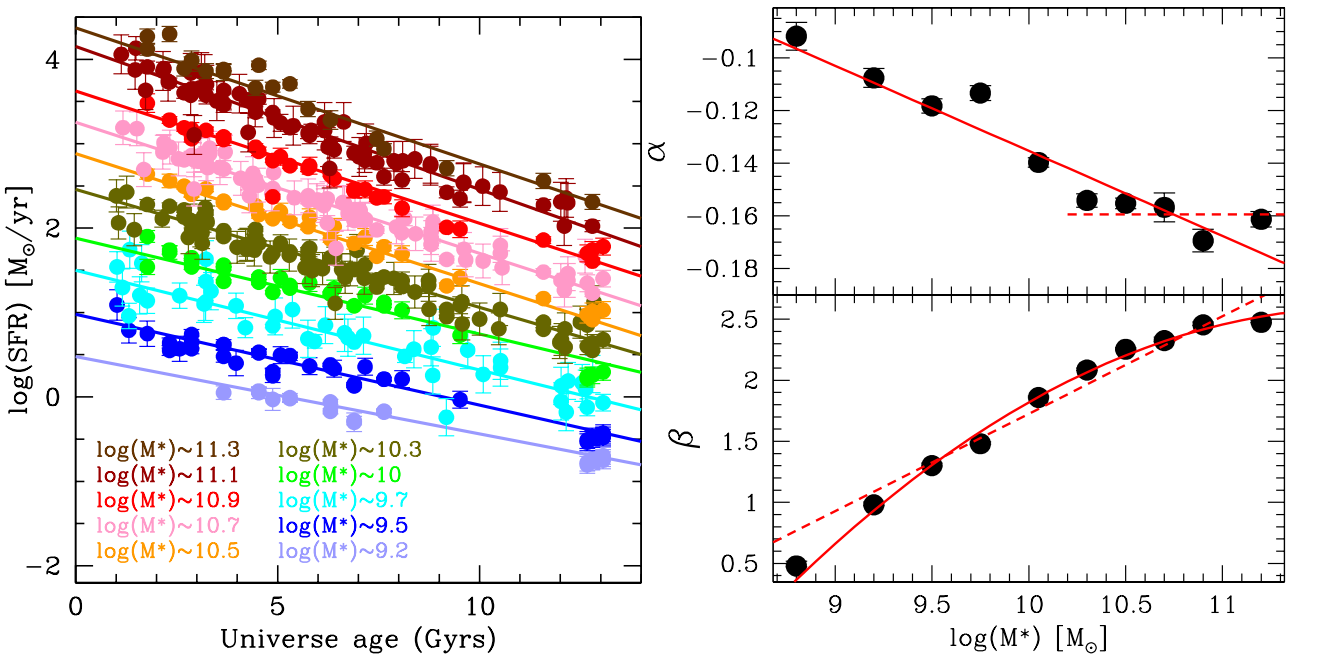

Figure 1. *Left panel:* logSFR versus Universe age in several bins of stellar masses. The data points indicate the SFR based on the MS estimates collected in this work. The solid lines show the best linear fit as in Eq. 9. Data points and lines are color-coded as a function of the stellar mass bin as indicated in the figure. For clarity, the relations are artificially displaced by 0.3 dex from one another. *Right panel:* $\alpha(logM_\star)$ (upper panel) and $\beta(logM_\star)$ (lower panel) as a function of $logM_\star$. The red solid lines in both panels indicate the best fit relations of Eq. 9. The dashed line in upper panel shows the consistency of non-evolution of the MS shape at the high stellar masses, as found in Popesso et al. (2019a). The dashed line in the bottom panel show the liner fit approximation as proposed in S14.

to larger MS slopes than the ones retrieved with other selection methods. One of the methods to retrieve blue sources is the Lyman break technique (Steidel et al. 1999; Stark et al. 2009; Bouwens et al. 2011), used to select high-z Lyman-break galaxies (LBGs). In the list of publications considered here only Tasca et al. (2015) apply the LBGs selection technique. Tomczak et al. (2016) compare the results of Tasca et al. (2015) with those based on the "mixed" selection method (see also discussion below) and find very good agreement. We conclude that the results of Tasca et al. (2015) seem less affected by the bias of the bluer selection discussed by S14. Similarly, Heinis et al. (2014) apply a UV selection to identify distant SFGs. Nevertheless, their estimates are not scattering significantly with respect to the other relations. Thus, we conclude that also in this case, the UV selection does not affect significantly the slope of the relation.

All other MS estimates included in our analysis are based on methods that S14 classify as "mixed". Such techniques include redder objects in the selection, thus considering also a large portion of the SFG population dominated by dust. These methods are considered to provide a more physical distinction between SFGs and quiescent galaxies (Ilbert et al. 2013; Schreiber et al. 2015). Among them we include the color-color selection based on the rest-frame (U-V) − (V-J) and (M_{NUV}-M_R) − (M_R-M_J) absolute colors, the 2σ clipping, the bimodality between SFGs and quiescent galaxies in the SFR-$M_\star$ plane. While these different selection methods do not seem to affect the average observed SFRs across different publications, as pointed out by S14, they do seem to influence the derived slopes and the intrinsic scatter of the MS. Popesso et al. (2019a) show that all these methods agree very well over most of the stellar mass range considered. However, small discrepancies can be observed due to little selection biases at very high stellar masses towards high redshift. Namely, selections as the (U-V) − (V-J) color selection tend to exclude part of the high mass star forming galaxies at relatively lower SFR with respect to the MS location. This would lead to a steeper MS at higher redshift with respect to the low redshift relation and thus a more significant evolution. The effect is an offset of ~0.15−0.2 dex at $M_\star$ of 10^{11} − $10^{11.5}$ $M_\odot$. Instead, the selection based on the (M_{NUV}-M_R) − (M_R-M_J) absolute colors is less prone to this selection bias, as it allows to select all galaxies populating the log-normal distribution around the MS location (Popesso et al. 2019a; Ilbert et al. 2015).

We point out that the MS estimates affected by this bias are the stacked points based on the CANDELS field dataset (Whitaker et al. 2014; Schreiber et al. 2015; Tomczak et al. 2016). Due to the very small volume sampled by the CANDELS fields, these include less than 15 galaxies per stacked point at stellar masses larger than 10^{11} $M_\odot$. Since this is below the limit required in Section 2, those stacked points are anyhow not included in our analysis.

3 FITTING THE MAIN SEQUENCE

In this work, we adopt two approaches to fit the MS relation. The first one follows S14 and consists in looking for the functional form that best describes the MS relation. As an alternative approach we investigate the functional form proposed by Lee et al. (2015), which has the advantage of being expressed with parameters that have a physical description. In the following procedure, after correcting stellar masses and SFRs with the calibration described above, we take into account the redshift and mass ranges of each study and we include in the fitting procedure only objects or stacked points actually observed at given mass and redshift without any extrapolation or interpolation. These mass ranges have either been taken directly from the paper in question or estimated based on the data included

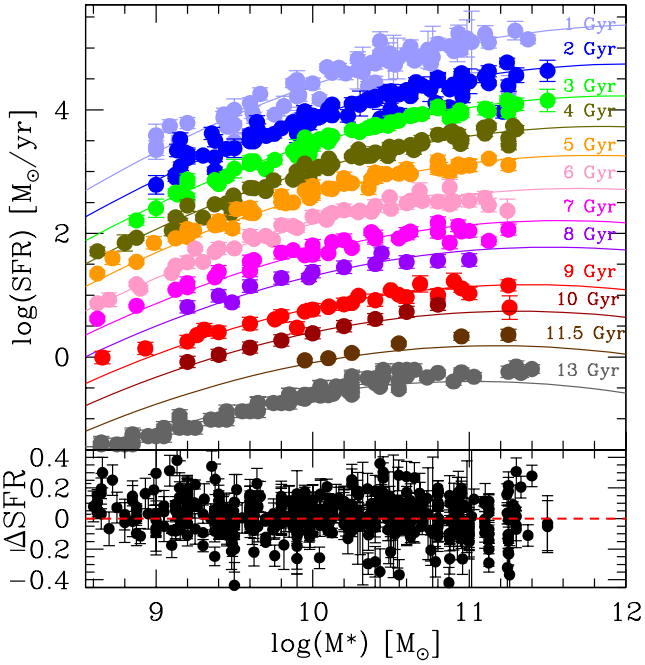

Figure 2. The upper panel shows the MS shape as a function of the Universe age from 2 to 13 Gyrs. The data points show the MS estimates collected and calibrated in this work. The solid lines indicate the best fit relation obtained with Eq. 10. Points and lines are color-coded as a function of time, as indicated in the panel. For clarity, the MS relations are artificially displaced by 0.3 dex from one another. The bottom panel shows the residual distribution as a function of stellar mass. The dashed red line shows the 0 level, corresponding to the best fit value.

in the relevant fits, rounded to the nearest 0.1 dex after excluding outlying points (see Appendix for a detailed description of the data taken from each publication).

3.1 S14 approach

In this Section we describe how we fit the MS and retrieve the functional form that best expresses the evolution of the slope and normalization as a function of time. We follow a revised version of the S14 approach. We proceed to fit the evolution of the SFR provided by each individual MS as function of time:

$$logSFR(t) = \alpha_i t + \beta_i, \quad (7)$$

The choice of fitting as a function of time rather than redshift is mainly practical, as a straightforward linear fit works very well for the time variable, while a more complicated functional form is required as a function of redshift.

By fitting α_i's and β_i's for a grid of $M_\star$, as shown in Fig. 1, we can derive a function of the form:

$$logSFR(t, logM_\star) = \alpha(logM_\star)t + \beta(logM_\star), \quad (8)$$

assuming a given parametrization for $\alpha(logM_\star)$ and $\beta(logM_\star)$.

As shown in the right panel of Fig. 1, the slope $\alpha(logM_\star)$ depends linearly on $logM_\star$, consistently with S14. Conversely, the best fitting form for $\beta(logM_\star)$ is not a simple linear dependence but it requires a quadratic form. This is because, differently for nearly all the MS compiled by S14, most of the MS estimates included here find a bending of the MS towards large stellar masses. Thus, the best fitting functions for $\alpha(logM_\star)$ and $\beta(logM_\star)$ are, respectively:

$$\alpha(logM_\star) = a_0 + a_1 logM_\star$$
$$\beta(logM_\star) = b_0 + b_1 logM_\star + b_2 log^2 M_\star \quad (9)$$

which gives:

$$logSFR(t, logM_\star) = (a_1 t + b_1) logM_\star + b_2 log^2 M_\star + (b_0 + a_0 t). \quad (10)$$

Eq. 10 differs from the best fitting function of S14 for the quadratic term $b_2 log^2 M_\star$, which is time independent. The slope of the MS is driven by the combination of the quadratic term and the linear term that sets the faint end slope, $(a_1 t + b_1) logM_\star$, which evolves with time. The normalization of the relation depends linearly on time through the term $(b_0 + a_0 t)$.

We use the functional form retrieved in Eq. 10 to fit the whole MS dataset without binning in stellar masses and time. The best fit parameters of Eq. 9 for $\alpha(logM_\star)$ and $\beta(logM_\star)$ are used as first guess for the fitting procedure. The final best fit parameters are given in Table 2 and the best fit MS is shown as a function of time in Fig. 2. The bottom panel shows the residual distribution of the MS estimates with respect to the best fit at given time and stellar mass. The scatter around the best fit is 0.06 dex. The MS is found to bend towards large stellar masses at all times due to the time independent quadratic term. The time variation of the faint end slope makes the relation steeper at early epochs. Nevertheless, the evolution of the slope is marginal after the first ~4 Gyrs, consistently with the results of S14, and as found in Popesso et al. (2019a). The normalization of the relation evolves consistently with the results of S14. We point out that it evolves roughly as $(1+z)^3$. However, this is only an approximation, because the SFR(z) can not be expressed accurately as a power law of $(1+z)$.

3.2 The MS turn-over

The approach of S14 is very effective in providing a good functional form for the MS. However, it is not trivial to physically interpret Eq.10. For this reason we explore a different approach by using the fitting function of Lee et al. (2015):

$$SFR(M_\star) = SFR_{max}/(1 + (M_\star/M_0)^{-\gamma}) \quad (11)$$

Unlike polynomial fits, as Eq. 10, the parameters of this model allow to quantify the interesting characteristics of the relation between stellar mass and SFR: *i)* γ, the power-law slope at low stellar masses, *ii)* M_0, the turnover mass, and *iii)* $logSFR_{max}$, the maximum value of $logSFR$ that the function asymptotically approaches at high stellar masses.

To capture the evolution of the MS through Eq. 11, we first fit the MS in bins of time to estimate the time dependence. This allows to obtain $S_0(t)$, $M_0(t)$ and $\gamma(t)$ to find the best functional form, which includes the time dependence in Eq. 11. The left panel of Fig. 3 shows the results of the best fit parameters as a function of time. We find that the exponent γ does not show any time dependence and it is consistent with the value -1. Both $logSFR_{max}$ and $logM_0$ depend linearly on time. Thus, they can be expressed as:

$$logSFR_{max}(t) = a_0 + a_1 t \quad (12)$$

and

$$logM_0(t) = a_2 + a_3 t \quad (13)$$

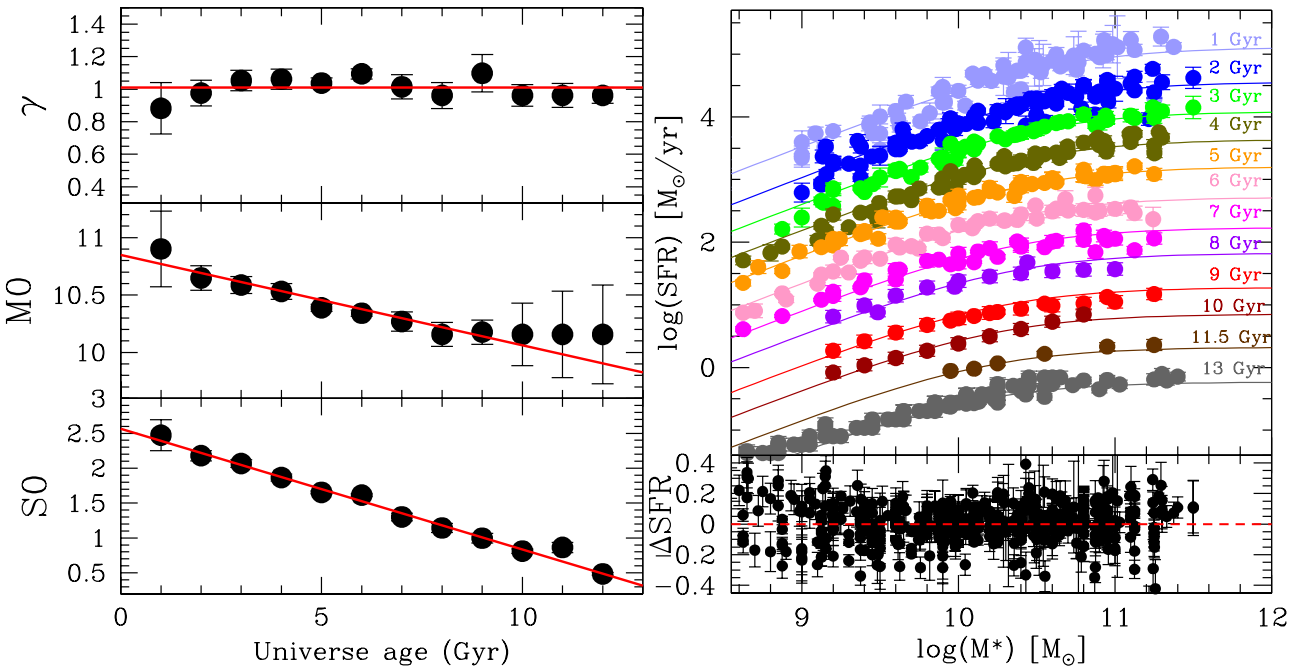

Figure 3. *Left panel:* evolution of γ (upper panel), $log M_0$ (central panel) and SFR_{max} (bottom panel) as a function of time. The red solid lines in each panel indicate the best fit relations of Eq. 12 and Eq. 13. *Right panel:* the upper panel shows the MS shape as a function of the Universe age from 2 to 13 Gyrs. The data points show the MS estimates collected and calibrated in this work. The solid lines indicate the best fit relation obtained with Eq. 14. Points and lines are color-coded as a function of time, as indicated in the panel. For clarity, the MS relations are artificially displaced by 0.3 dex from one another. The bottom panel shows the residual distribution as a function of stellar mass. The dashed red line shows the 0 level, corresponding to the best fit value.

By taking into account such evolution, we can write Eq. 11 as a function of time as:

$$logSFR(M_\star, t) = a_0 + a_1 t - log(1 - (M_\star/10^{a_2+a_3 t})^{-a_4} \quad (14)$$

We use this functional form to fit the MS estimate dataset as a function of mass and time without any binning. The results of the best fitting procedure are indicated in Table 2. The right panel of Fig. 3 shows the MS data points as a function of time with the best fitting curves. The scatter around the best fit is 0.07 dex, indicating that also Eq. 14 provides an excellent fitting function for the evolution of the MS. Consistently with the results obtained with the functional form given by Eq. 10, the MS bends at the high mass end with a turn-over mass that is evolving with time. The exponent γ does not evolve with time and it is consistent with the value -1. This implies that the MS is well represented by the functional form:

$$SFR(M_\star) = SFR_{max}(t)/(1 + (M_0(t)/M_\star)) \quad (15)$$

which is regulated by only two parameters, $M_0(t)$ and $SFR_{max}(t)$. We estimate the best fit parameters also for this functional form. The results are included in Table 2. The evolution of the MS shape is regulated by the change of the turn-over mass $M_0(t)$. This changes of only 25% over the past 9-10 Gyrs, and is a factor of 2 larger in the first 3-4 Gyrs. The normalization of the relation, set by $SFR_{max}(t)$ parameter, exhibits the strongest evolution and it is consistent within 1σ with the value found for the normalization in Eq. 10.

3.3 Towards a physical explanation of the MS shape evolution

Given Eq. 15, $M0(t)$ can be interpreted as the mass thresholds between two regimes. At $M_\star << M_0(t)$ the sSFR of galaxies is nearly constant as a function of stellar mass and equal to $\sim SFR_{max}(t)/M_0(t)$. At $M_\star >> M_0(t)$, the sSFR is progressively suppressed as it is approximated by $SFR_{max}(t)/M_\star$. Thus, the turn-over stellar mass separates a regime of constant star formation rate per unit of stellar mass from a regime of SFR suppression.

Eq. 10		Eq. 14		Eq. 15	
a0	0.26±0.03	a0	2.62±0.05	a0	2.61±0.05
a1	-0.04±0.01	a1	-0.17±0.05	a1	-0.14±0.04
b0	-27.58±0.05	a2	10.66±0.01	a2	10.73±0.01
b1	4.95±0.02	a3	-0.042±0.02	a3	-0.043±0.02
b2	-0.20±0.02	a4	0.98±0.01	a4	1

Table 2. The table lists the best fit parameters of Eq.10, Eq. 14 in the first 2 columns. The last column lists the best fit parameters of Eq. 15, which corresponds to Eq. 14 with the slope $a4 = -1$ (γ in Eq. 11).

Popesso et al. (2019b) point out, exploiting the halo mass catalog of Yang et al. (2007), that at z~0 the region of the MS (within 3σ from the relation) is completely dominated by central galaxies. Due to the rather tight correlation between the central galaxy stellar mass and the host halo mass (Mh), this implies that the SFG mean host halo mass is increasing along the MS with $M_\star$. Up to z~1.3 we are able to check if this holds by exploiting the cosmic web catalog of Darvish et al. (2017) in the COSMOS field. This is based on the accurate photometric redshifts of the COSMOS15 catalog (Laigle et al. 2016) to identify clusters, groups and filaments and assign a membership probability to each galaxy up to $z \sim 1.3$ and down to stellar masses of 10^9 $M_\odot$. For galaxies with high probability to be in groups and clusters, the catalog provides also a classification in central and satellite galaxies, by identifying as central the most massive system. We use the IR selected galaxy catalog of Popesso

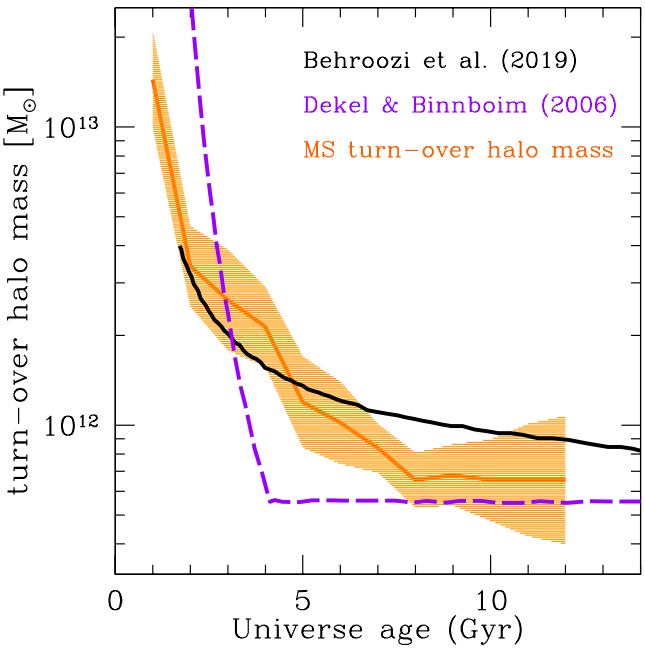

Figure 4. Evolution of the host halo turn-over mass (orange line) as a function of the Universe Age. The solid black line indicates the evolution of the quenching halo mass of Behroozi et al. (2019). The dashed magenta line shows the evolution of the halo mass threshold between cold and hot accretion regime of Dekel & Birnboim (2006).

et al. (2019a) in the COSMOS field, based on the combination of *Herschel* and *Spitzer* MIPS data, to check the central galaxy fraction in the MS region in the redshift window explored by Darvish et al. (2017). The SFR of each galaxy is given by the combination of the UV and IR contribution (Popesso et al. 2019b). The MS is identified as the region within 3σ from the MS relation given by Eq. 14 in several redshift bins. We assume $\sigma = 0.3$ dex. At all redshifts up to $z = 1.3$, the MS region turns out to be dominated by central galaxies, which account for 70% of the galaxy population. To check whether the MS region is dominated by central galaxies also at z>1.3, we use the predictions from the Illustris TNG hydro-dynamical simulation (Pillepich et al. 2018). In this case we use as reference the MS determined as in Donnari et al. (2019) on the same data. Also in this case, as expected, central galaxies account for 70-80% of the galaxy population at $z > 1.3$. Thus, is it plausible to assume that the MS is dominated by central galaxies also in the distant Universe.

This aspect is crucial, because it allows us to convert the turn-over stellar mass of the SFG MS into a *turn-over host halo mass*, thanks to the correlation between central galaxy stellar mass and host halo mass (Yang et al. 2007; Behroozi et al. 2013; Behroozi et al. 2019). In particular, we use the results of the empirical model UNIVERSEMACHINE of Behroozi et al. (2019) to convert $M_0(t)$ into host halo turn-over mass $M_{h0}(t)$. In Fig. 4 we plot the evolution of $M_{h0}(t)$ as a function of time together with the halo mass quenching threshold derived in Behroozi et al. (2019), and the evolution of the transition mass between cold and hot accretion predicted by the theory of mass accretion as in Dekel & Birnboim (2006). The halo mass quenching threshold is defined as the halo mass above which the fraction of quenched galaxies is larger than 50%. The hot/cold transition, instead, is defined as the halo mass at which the cold gas streams coming from the cosmic web filaments are no longer able to penetrate the halo and feed the central galaxy. The curve of Dekel & Birnboim (2006) depends on the halo temperature, but it predicts that at higher redshift ($z > 2.5-3$) cold gas streams are still able to penetrate massive hot halos. Thus, it represents the threshold between hot and cold gas accretion onto the central galaxy. The evolution of M_{h0} with time lies between the predictions of the empirical model of Behroozi et al. (2019) and the theoretical model of Dekel & Birnboim (2006). The evolution of $M_{h0}(t)$ is steeper with respect to the quenching halo mass evolution. It is consistent within 1σ with the prediction of Dekel & Birnboim (2006) in the last 4 Gyrs but it does not exhibit the same drastic change in slope around 4 Gyrs of Universe age. Behroozi et al. (2019) discuss that the disagreement between the empirical and the theoretical predictions might originate from the non inclusion of the effects of black hole feedback in the treatment of accretion. This, indeed, might play an important role in affecting the thermodynamical conditions of the circum-galactic-medium (CGM) of the central galaxy, mainly by injecting large quantities of energy into it (Weinberger et al. 2017; Nelson et al. 2019). We suggest that the turn-over mass of the MS might be indicative of the transition between an environment that efficiently sustains the star formation process of the central galaxies, e.g. through cold gas streams, to one which is hostile to the star formation process due to the suppression of the feeding mechanism of the central galaxy. This suppression might originate, as suggested by nearly all the most sophisticated hydrodynamical simulations, by the interplay between the hot gas in massive halos and central black hole feedback (Voit et al. 2015, 2017; Weinberger et al. 2017; Nelson et al. 2019).

4 COMPARISON WITH PREVIOUS RESULTS

In this Section we compare our results on the evolution of the MS with previous observational and theoretical results.

We first compare our results to the ones of S14, keeping in mind that the analysis of S14 is limited to the stellar mass range $10^{9.7} - 10^{11.1}$ $M_\odot$. In Fig. 5 we plot in magenta the homogenised collection of MS relations in seven different redshift bins. The purple solid line marks our best-fit estimates at the given redshift, as expressed in Eq. 14. The MS relation of S14 is indicated with the solid green line, while its extrapolation at lower/larger stellar masses is shows as a dashed line. We find very good agreement between the two results. S14 claim that they do not find a bending of the MS at the high mass end. However, we point out that this could be due to the limited stellar mass range considered in the fitting procedure. Indeed, while a single power law might be a good approximation over this range, the extrapolation to larger masses shows that such functional form does not reproduce at every redshift the observations at stellar masses larger than 10^{11} $M_\odot$.

Fig. 5 shows also the comparison between our results and the predictions of the Illustris TNG300 simulation (Pillepich et al. 2018). TNG300 is the largest volume simulated in the suite of Illustris TNG hydrodynamical simulations. The choice of TNG300 is driven by the need to sample a sufficiently large volume to capture the rare giant star forming galaxies at the high mass end of the MS. The SFRs are averaged over 200 Myr and measured within a physical aperture of $2R_{star}$, where R_{star} is stellar half mass radius (see also Donnari et al. 2019). The shaded region in Fig. 5 shows the distribution of the IllustrisTNG galaxies, color coded according to the galaxy number density in bins of SFR and $M_\star$. The IllustrisTNG MS is estimated as a running mean as a function of $M_\star$ and it is indicated by the orange yellow line. We also show in yellow the MS of Donnari et al. (2019), which is estimated up to $z \sim 2$ by mocking

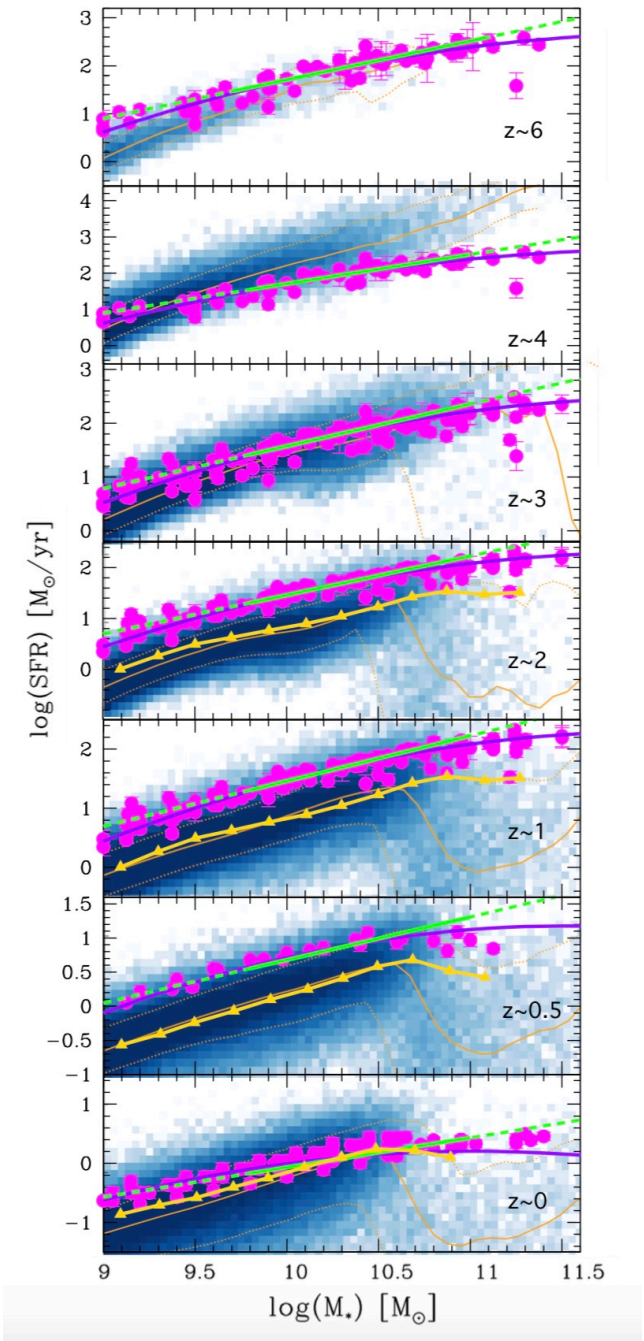

Figure 5. MS of star forming galaxies in several redshift bins from $z \sim 6$ to $z \sim 0$. The shaded blue region in each panel indicate the distribution of simulated Illustris TNG galaxies in the SFR-stellar mass plane. The blue scale is according to the number density of galaxies. The orange line show the running median in bins of stellar mass for the simulated galaxies, while the connected yellow triangles show the relation of Donnari et al. (2019) limited to the UVJ selected galaxies in Illustris TNG. The magenta points show the data collected in this paper and the purple solid line indicates our best fit according to Eq. 14. The solid green line shows the best fit of S14 in the analysed stellar mass range, and the green dashed line shows its extrapolation to lower and larger stellar masses.

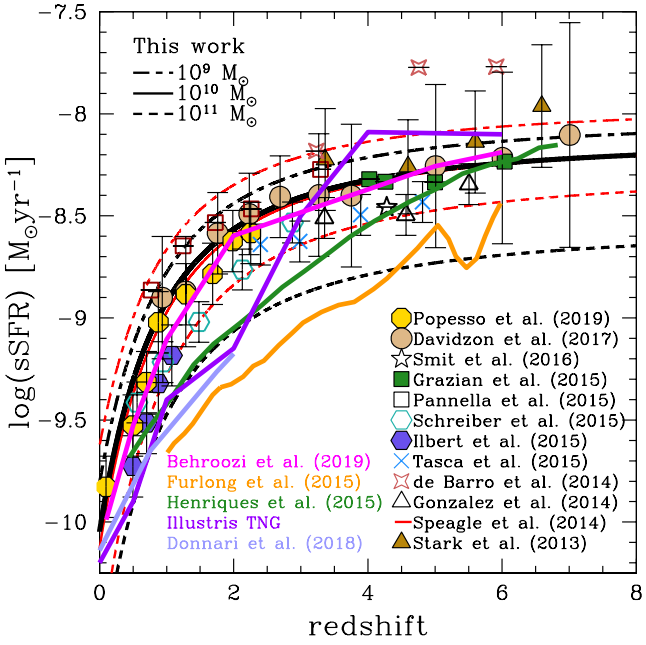

Figure 6. Evolution of sSFR as a function of redshift. The black lines show the sSFR evolution given by the best fit of Eq. 14 at three stellar mass values: 10^9 (dot-dashed line), 10^{10} (solid line) and 10^{11} $M_\odot$ (dashed line). We provide the same relation for the S14 best fit (red lines). We plot for comparison the data of several works in literature with symbols indicated in the figure. The yellow, green, purple and light purple solid lines show the predictions of EAGLE simulation of Furlong et al. (2015), The MUNICH simulation of Henriques et al. (2015), the Illustris TNG as estimated here and the one of Donnari et al. (2019), respectively. The magenta solid line shows the best fitting model of Behroozi et al. (2019).

the UVJ selection of Whitaker et al. (2012). The two estimates agree remarkably well up to stellar masses of $\sim 10^{10.5}$ $M_\odot$ and diverge at larger stellar masses, where the UVJ selection of Donnari et al. (2019) exclude most of the low SFR systems.

We notice a good agreement between the IllustrisTNG predictions and our results at early epochs ($z \sim 6$). The observed MS lies over the simulated relation. However, no giant star forming galaxies are observed at all in the TNG300 volume at $z \sim 6$ above $10^{10.5}$ $M_\odot$. The observations, instead, indicate that such galaxies populate the high mass end of the relation, in agreement with the results of the GSMF of active galaxies of Davidzon et al. (2017).

Massive star forming galaxies appear in the TNG simulation only between $z \sim 4$ to ~ 3, with a larger SFR compared to observations, in particular at $z \sim 4$. At this epoch the predicted and observed low mass slope (below stellar masses of $10^{10.5}$ $M_\odot$) are in agreement within 1σ. At later epochs ($z < 2$), the predicted MS is systematically below the observations by ~ 0.5 dex, according to the results of Donnari et al. (2019). Observations and predictions are again in agreement at $z \sim 0$ up to 10^{11} $M_\odot$. Above this mass no more SFGs are detected in the simulations at odds with observations.

We provide in Fig. 6 a comparison of the sSFR evolution with simulations, as well as other works in literature. We plot the evolution of the sSFR derived from the best fit of Eq. 14 and from S14 in black and red, respectively, both computed in three different stellar mass bins: 10^9 (black dot-dashed line), 10^{10} (black solid line) and 10^{11} $M_\odot$ (black dashed line). The black and red lines overlap at 10^{10} $M_\odot$ and are relatively in agreement at 10^9 $M_\odot$, but differ by more

than 2σ at 10^{11} $M_{\odot}$, as expected. The prediction of IllustrisTNG, up to $z \sim 6$, those from Donnari et al. (2019), up to $z \sim 2$, as well as the best fit of the empirical model UNIVERSEMACHINE (Behroozi et al. 2019), all computed for $M_{\star} = 10^{10}$ $M_{\odot}$, are shown in purple, lavander and magenta, respectively. The simulated data of Illustris TNG are in agreement with observations at high redshift and in the local Universe, but the slope of the predicted sSFR evolution is steeper than observations, as pointed out above from the MS comparison. The redshift evolution of sSFR obtained from Behroozi et al. (2019) is perfectly overlapping with observations at the same stellar mass. Finally, we show in Fig. 6 the redshift evolution of the sSFR obtained from the EAGLE hydrodynamical simulation (Furlong et al. 2015) and the latest Munich simulation (Henriques et al. 2015). Both simulated data are below the observations and exhibit a steeper relation. However, we point out that, as discussed by Davidzon et al. (2018), such comparison is complicated by the fact that simulated galaxies are not selected to be SFGs. Thus, the slope and normalization of the sSFR-redshift relation is biased by quiescent galaxies.

We conclude that the star formation activity of simulated TNG galaxies is declining much faster than in observations between redshift ~ 3 and ~ 0. This leads to a MS normalization too low with respect to observations in the same redshift window. The disagreement is more significant in particular for the most massive systems above 10^{11} $M_{\odot}$. As discussed in Donnari et al. (2019), this might point to some fundamental limitations in our understanding of the processes governing the star formation evolution in galaxies, or to some observational bias (or a combination of these two aspects). As pointed out by Davidzon et al. (2018), the disagreement below z~3 between observations and simulations is still significant after accounting for several possible biases (discrepancies in the SFR time scale estimate, in the physical region used to measure stellar masses and SFRs and in the stellar mass loss assumption of the SPS model between simulations and observations). This might suggest that the supernovae and black hole feedback implemented in the IllustrisTNG (see Weinberger et al. 2017 for more details) are still too efficient in suppressing the star formation activity of galactic systems.

5 SUMMARY AND CONCLUSION

We compile a collection of the most important publications regarding the evolution of the MS of star forming galaxies in the widest range of redshift ($0 < z < 6$), stellar mass ($10^{8.5} - 10^{11.5}$ $M_{\odot}$) and SFR ($0 - 500$ $M_{\odot} yr^{-1}$) ever probed. We convert all observations to a common calibration to study the evolution of the relation with different approaches. We find a remarkable good agreement between the different estimates at any stellar mass and time. The resulting MS exhibits a curvature towards the high stellar masses, which is slowly evolving with time. We provide two functional forms, which take into account the time evolution of the MS normalization and slope. Following the approach of S14, we estimate the best polynomial fitting form in the logSFR−log$M_{\star}$ space, by studying the evolution with time of the logSFR at fixed stellar mass. A second order polynomial form is well representing the relation, with a non evolving quadratic term and an evolving normalization and linear term. The normalization is evolving as a power law of the Universe age. The slow evolution of the linear term reproduces the steepening of the relation towards the first 3-4 Gyrs of the Universe. We provide as alternative fitting form the one of Lee et al. (2015), which has the advantage of being expressed by physical parameters. These are the low mass slope, the normalization and the turn-over mass ($M_0(t)$). While the slope does not evolve with time, normalization and turn-over mass evolve as a power law of the Universe age. The turn-over mass, in particular, determines the MS shape. It marginally evolves with time, and it is responsible for the steepening of the relation towards $z \sim 4 - 6$. At stellar masses below $M_0(t)$, SFGs have a constant sSFR, while above $M_0(t)$ the sSFR is suppressed. As the MS region is dominated by central galaxies, we use the relation between central galaxy stellar mass and host halo mass to convert $M_0(t)$ into a "turn-over host halo mass". We find that its evolution is consistent with the one of the halo mass threshold between cold and hot accretion regimes or the quenching halo mass defined by Behroozi et al. (2019). This might indicate that $M_0(t)$ defines the transition between an environment able to sustain the SF process of the central galaxy, for instance through cold gas streams as predicted by Dekel & Birnboim (2006), to a regime hostile to the same process. The latter might be the result of the interplay between the hot gas in massive halos and the black hole feedback generated by the central galaxy itself.

The comparison of our results with the IllustrisTNG simulation shows that the simulated MS shape is qualitatively consistent with the observations. However, the normalization of the simulated relation is systematically lower by at least 0.5 dex with respect to observations at $z < 3$. As a consequence the sSFR of SFGs evolves more rapidly in TNG galaxies than in observed ones. This might suggest that the feedback implemented in the IllustrisTNG is likely too efficient in suppressing the star formation activity of galactic systems.

ACKNOWLEDGEMENTS

This research was supported by the DFG cluster of excellence "Origin and Structure of the Universe" (www.universe-cluster.de).

REFERENCES

Behroozi P. S., Wechsler R. H., Conroy C., 2013, The Astrophysical Journal, 770, 57
Behroozi P., Wechsler R. H., Hearin A. P., Conroy C., 2019, MNRAS, 488, 3143
Belfiore F., et al., 2018, MNRAS, 477, 3014
Bourne N., et al., 2017, MNRAS, 467, 1360
Bouwens R. J., et al., 2011, ApJ, 737, 90
Brinchmann J., Charlot S., White S. D. M., Tremonti C., Kauffmann G., Heckman T., Brinkmann J., 2004, Monthly Notices of the Royal Astronomical Society, 351, 1151
Bruzual G., Charlot S., 2003, Monthly Notices of the Royal Astronomical Society, 344, 1000
Bundy K., et al., 2015, The Astrophysical Journal, 798, 7
Calzetti D., Armus L., Bohlin R. C., Kinney A. L., Koornneef J., Storchi-Bergmann T., 2000, The Astrophysical Journal, 533, 682
Chang Y.-Y., van der Wel A., da Cunha E., Rix H.-W., 2015, ApJS, 219, 8
Charlot S., Fall S. M., 2000, ApJ, 539, 718
Chen Y.-M., Wild V., Kauffmann G., Blaizot J., Davis M., Noeske K., Wang J.-M., Willmer C., 2009, MNRAS, 393, 406
Daddi E., et al., 2007, The Astrophysical Journal, 670, 156
Dale D. A., et al., 2009, ApJ, 703, 517
Darvish B., Mobasher B., Martin D. C., Sobral D., Scoville N., Stroe A., Hemmati S., Kartaltepe J., 2017, ApJ, 837, 16
Davidzon I., et al., 2017, A&A, 605, A70
Davidzon I., Ilbert O., Faisst A. L., Sparre M., Capak P. L., 2018, ApJ, 852, 107

Dekel A., Birnboim Y., 2006, Monthly Notices of the Royal Astronomical Society, 368, 2
Donnari M., et al., 2019, MNRAS, 485, 4817
Dunlop J. S., et al., 2017, MNRAS, 466, 861
Elbaz D., et al., 2007, Astronomy & Astrophysics, 468, 33
Elbaz D., et al., 2011, Astronomy & Astrophysics, 533, A119
Erfanianfar G., et al., 2016, Monthly Notices of the Royal Astronomical Society, 455, 2839
Furlong M., et al., 2015, MNRAS, 450, 4486
Heinis S., et al., 2014, MNRAS, 437, 1268
Henriques B. M. B., White S. D. M., Thomas P. A., Angulo R., Guo Q., Lemson G., Springel V., Overzier R., 2015, MNRAS, 451, 2663
Ilbert O., et al., 2013, A&A, 556, A55
Ilbert O., et al., 2015, Astronomy & Astrophysics, 579, A2
Karim A., et al., 2011, The Astrophysical Journal, 730, 61
Kashino D., et al., 2013, The Astrophysical Journal Letters, 777, L8
Kennicutt R. C., Evans N. J., 2012, ARA&A, 50, 531
Kurczynski P., et al., 2016, ApJ, 820, L1
Laigle C., et al., 2016, ApJS, 224, 24
Le Fèvre O., et al., 2015, A&A, 576, A79
Lee K.-S., et al., 2012, The Astrophysical Journal, 752, 66
Lee N., et al., 2015, ApJ, 801, 80
Lee B., et al., 2018, ApJ, 853, 131
Leslie S. K., et al., 2020, ApJ, 899, 58
Lutz D., 2014, ARA&A, 52, 373
Magdis G. E., Elbaz D., Daddi E., Morrison G. E., Dickinson M., Rigopoulou D., Gobat R., Hwang H. S., 2010, ApJ, 714, 1740
Meurer G. R., Heckman T. M., Calzetti D., 1999, The Astrophysical Journal, 521, 64
Moustakas J., et al., 2013, ApJ, 767, 50
Nelson D., et al., 2019, MNRAS, p. 2010
Noeske K. G., et al., 2007, The Astrophysical Journal, 660, L47
Nordon R., et al., 2010, arXiv.org, p. L24
Oemler Augustus J., Abramson L. E., Gladders M. D., Dressler A., Poggianti B. M., Vulcani B., 2017, ApJ, 844, 45
Oliver S., et al., 2010, MNRAS, 405, 2279
Oliver S. J., et al., 2012, MNRAS, 424, 1614
Pannella M., et al., 2009, arXiv.org, pp L116–L120
Pearson W. J., et al., 2018, A&A, 615, A146
Peng Y.-j., et al., 2010, The Astrophysical Journal, 721, 193
Pillepich A., et al., 2018, MNRAS, 473, 4077
Popesso P., et al., 2019a, MNRAS, p. 2263
Popesso P., et al., 2019b, MNRAS, 483, 3213
Reddy N., et al., 2012, ApJ, 744, 154
Renzini A., Peng Y.-j., 2015, The Astrophysical Journal Letters, 801, L29
Robert C Kennicutt J., 1998, arXiv.org, pp 189–232
Rodighiero G., et al., 2011, The Astrophysical Journal Letters, 739, L40
Rodighiero G., et al., 2014, arXiv.org, pp 19–30
Salim S., et al., 2007, The Astrophysical Journal Supplement Series, 173, 267
Salim S., et al., 2016, ApJS, 227, 2
Salmi F., Daddi E., Elbaz D., Sargent M., Dickinson M., Renzini A., Bethermin M., Le Borgne D., 2012, arXiv.org, p. L14
Santini P., et al., 2009, A&A, 504, 751
Santini P., et al., 2017, ApJ, 847, 76
Schreiber C., et al., 2015, Astronomy & Astrophysics, 575, A74
Shim H., Chary R.-R., Dickinson M., Lin L., Spinrad H., Stern D., Yan C.-H., 2011, ApJ, 738, 69
Shivaei I., Reddy N. A., Steidel C. C., Shapley A. E., 2015, ApJ, 804, 149
Sobral D., Best P. N., Smail I., Mobasher B., Stott J., Nisbet D., 2014, MNRAS, 437, 3516
Speagle J. S., Steinhardt C. L., Capak P. L., Silverman J. D., 2014, arXiv.org, p. 15
Spergel D. N., et al., 2003, ApJS, 148, 175
Stark D. P., Ellis R. S., Bunker A., Bundy K., Targett T., Benson A., Lacy M., 2009, ApJ, 697, 1493
Steidel C. C., Adelberger K. L., Giavalisco M., Dickinson M., Pettini M., 1999, ApJ, 519, 1
Steinhardt C. L., et al., 2014, The Astrophysical Journal Letters, 791, L25
Tasca L. A. M., et al., 2015, A&A, 581, A54
Tomczak A. R., et al., 2016, ApJ, 817, 118
Valiante E., et al., 2016, MNRAS, 462, 3146
Voit G. M., Bryan G. L., O'Shea B. W., Donahue M., 2015, ApJ, 808, L30
Voit G. M., Meece G., Li Y., O'Shea B. W., Bryan G. L., Donahue M., 2017, ApJ, 845, 80
Weinberger R., et al., 2017, MNRAS, 465, 3291
Whitaker K. E., van Dokkum P. G., Brammer G., Franx M., 2012, The Astrophysical Journal Letters, 754, L29
Whitaker K. E., et al., 2014, The Astrophysical Journal, 795, 104
Yang X., Mo H. J., van den Bosch F. C., Pasquali A., Li C., Barden M., 2007, The Astrophysical Journal, 671, 153
Zahid H. J., Bresolin F., Kewley L. J., Coil A. L., Davé R., 2012, ApJ, 750, 120
da Cunha E., Charlot S., Elbaz D., 2008, MNRAS, 388, 1595

APPENDIX A: THE SELECTED MS

Here we list and describe the MS estimates included in the analysis and the data they are based on:

- Speagle et al. (2014) do not provide the collection of data used for calibrating the average MS estimates but only the best fits. A large number of best fits are provided based on different subsamples, depending on the star forming galaxy selection method, and on the range of stellar masses and cosmic time included in the fit. We use in this paper the fit n. 64 based on a "mixed selection", which S14 consider as more inclusive of the SFG population (see Section 2.3 for a detailed discussion). The fit is restricted to stellar masses between $10^{9.7}$ $M_\odot$ and $10^{11.1}$ $M_\odot$ and it excludes the first 2 Gyrs of the Universe Age. In order to properly populate the S14 MS given by the fit n. 64, we use the data of their Fig n. 4, which shows the value of the SFR as a function of time in 4 stellar mass bins. We distribute randomly the data within the stellar mass bins and use the time information to estimate the SFR as a function of stellar mass and time in the range $10^{9.7} - 10^{11.1}$ $M_\odot$ and 2-12 Gyrs of Universe age. The SFRs obtained in this way are calibrated to the KE12 calibration and a Kroupa IMF.
- Rodighiero et al. (2014) provide the MS estimate of BzK selected galaxies in the redshift bin $1.4 < z < 2.5$ in the COSMOS field , on the basis of various SFR indicators including UV emission, $H\alpha$ emission, MIR and FIR emission. In this analysis we use the four data-points obtained through the stacking analysis of the BzK sample in the COSMOS PACS maps in the stellar mass range $10^{10} - 10^{11.5}$ $M_\odot$. The SFR and stellar masses are obtained with a Salpeter IMF and are corrected to the KE12 calibration and a Kroupa IMF.
- Heinis et al. (2014) provide the MS based on the stacking UV selected SFGs in bins of FUV luminosity in the HerMES maps (Oliver et al. 2012). The derived SFR is based on the combination of NUV and IR luminosities, with a Chabrier IMF. The IMF is estimated between $10^{9.5}$ and $10^{11.3}$ $M_\odot$ at $z \sim 1.5$, $z \sim 3$ and $z \sim 4$. We include in our analysis the stacked points at the observed stellar masses and redshift given in the paper.
- Whitaker et al. (2014) provide the MS based on stacking of UVJ selected star forming galaxies on *Spitzer* MIPS 24 μm data in the 3D-HST CANDELS fields. The derived SFR is based on the combination of NUV and IR luminosities, with a Chabrier IMF. The considered redshift range is 0.5-2.5 and the MS is estimated in the following stellar mass and redshift ranges: $10^{8.5} - 10^{11.2}$ $M_\odot$ at $0.5 < z < 1$, $10^{9} - 10^{11.3}$ $M_\odot$ at $1 < z < 1.5$, $10^{9.2} - 10^{11.5}$ $M_\odot$ at $1.5 < z < 2$ and $10^{9.3} - 10^{11.5}$ $M_\odot$ at $2 < z < 2.5$. We include

in our analysis the stacked points at the observed stellar masses and redshift given in the paper.

• Chang et al. (2015) provide SFR based on SED fitting results of MAGHPHYS code, from GALEX to WISE data in the local Universe. As already reported by Popesso et al. (2019b), the catalog provides SFRs underestimated with respect to the Hα based and IR based SFR estimates. Salim et al. (2016) discuss that this is likely due to the fact that the MAGHPHYS SED fitting results are mostly driven by the higher SNR 12 μm WISE data-point than the low SNR 22 μm WISE data, leading to artificially low SFR. Chang et al. (2015) report that their MS at $z < 0.1$ is systematically lower (0.15 dex) with respect to other Hα and IR based MS. We estimate the MS by using the best fit relation in stellar mass bins of 0.25 dex to take into account stellar mass uncertainties and after correcting for the 0.15 dex offset.

• Lee et al. (2015) use a ladder of SFR indicators to study the MS in the COSMOS field at $0.3 < z < 1.3$. Due to the flux limit of the *Spitzer* MIPS 24 μm and *Herschel* PACS and SPIRE catalog, the combination of NUV and IR luminosities provide the SFR only for highly star forming objects (starburst and massive SFGs). For less active or less dusty objects they use dust corrected NUV luminosities (see their Fig. 3 for the contribution of any SFR indicator as a function of stellar mass). Star forming galaxies are selected according to their (M_{NUV}-M_R) − (M_R-M_J) colors with a Chiabrier IMF. The MS is estimated as the median SFR value in equally populated bins of stellar mass in the following ranges: $10^{8.5} - 10^{11.}$ $M_\odot$ at $z = 0.36$, $10^{9} - 10^{11.}$ $M_\odot$ at $z = 0.55$, $10^{9} - 10^{11.}$ $M_\odot$ at $z = 0.70$, and between $10^{9.3}$ and $10^{11.2}$ $M_\odot$ at $z = 0.85$, $z = 0.99$ and $z = 1.19$. We include in our analysis the median points at the observed stellar masses and redshift.

• Ilbert et al. (2015) use the flux limited sample of *Spitzer* MIPS 24 μm and *Herschel* PACS and SPIRE of the COSMOS field to study the distribution of galaxies in the SFR-stellar mass plane. Galaxies are further selected according to their (M_{NUV}-M_R) − (M_R-M_J) colors. The SFR is estimated with a combination of NUV and IR luminosities. The MS is identified as the peak of the SFR distribution at several stellar mass bins at stellar masses above 10^{10} $M_\odot$ and in the redshift range $0.2 < z < 1.4$. This corresponds to the median SFR in a log-normal distribution. We include in our analysis the median points at the observed stellar masses and redshift given in the paper.

• Tasca et al. (2015) use the spectroscopically selected sample of the VIMOS Ultra Deep Survey (VUDS, Le Fèvre et al. 2015). Galaxies are selected from a combination of photometric redshifts, as well as from color selection criteria like LBG, combined with a flux limit $22.5 < i_{AB} < 25$. The SFR is derived via SED fitting techniques with *Le Phare*, assuming the BC03 SPS model, a Chabrier IMF and a Calzetti et al. (2000) extinction law. The MS is provided in the following stellar mass and redshift ranges: $10^{7.5} - 10^{10}$ $M_\odot$ at $0 < z < 0.7$, $10^{8.5} - 10^{11}$ $M_\odot$ at $0.7 < z < 1.5$, $10^{9} - 10^{11}$ $M_\odot$ at $1.5 < z < 2.5$ and at $2.5 < z < 3.5$, $10^{9.3} - 10^{10.6}$ $M_\odot$ at $3.5 < z < 4.5$ and $10^{9} - 10^{11}$ $M_\odot$ at $z > 4.5$. We include in our analysis the mean points at the observed stellar masses and redshift, as given in the paper.

• Renzini & Peng (2015) provide a fit of the local MS at $z < 0.085$ in the stellar mass range $10^{9} - 10^{10.5}$ $M_\odot$. The SFR is based on dust corrected SDSS Hα fluxed for systems classified as star forming in the BPT diagram and through the D4000 break for non active systems or AGN hosts (Brinchmann et al. 2004). SFR and stellar masses are estimated with a Chabrier IMF. The MS is identified as the peak of the SFR distribution at fixed stellar mass in the SFR-stellar mass plane. This corresponds to the median SFR in a log-normal distribution. We estimate the MS by using the best fit relation in stellar mass bins of 0.25 dex to take into account stellar mass uncertainties.

• Schreiber et al. (2015) perform a stacking analysis of UVJ selected galaxies in the deep *Herschel* PACS maps of the CANDELS fields. The mean IR luminosity derived for the stacks is combined with the mean FUV luminosity to derive the SFR. SFR and stellar masses are estimated with a Salpeter IMF. The MS is given in the following stellar mass and redshift ranges: $10^{9} - 10^{11}$ $M_\odot$ at $z \sim 0.5$, $z \sim 1$ and $z \sim 1.6$, $10^{9.8} - 10^{11}$ $M_\odot$ at $z \sim 2$ and $z \sim 3$. We include in our analysis the stacked points at the observed stellar masses and redshift, as given in the paper.

• Erfanianfar et al. (2016) provide the MS at $z < 1.1$. The SFR is based on the flux limited sample of *Spitzer* MIPS 24 μm and *Herschel* PACS and SPIRE available in the ECDFS and COSMOS fields. The SFR is derived from the far-IR flux with a Chabrier IMF. The MS is retrieved via σ-clipping. It is estimeted in the stellar mass range $10^{9} - 10^{11.5}$ at $0.15 < z < 0.5$ and $0.5 < z < 1.1$. We include in our analysis the stacked points at the observed stellar masses and redshift, as given in the paper.

• Tomczak et al. (2016) perform a stacking analysis of UVJ selected galaxies in the deep *Herschel* maps of the CANDELS fields. The mean IR luminosity derived for the stacks is combined with the mean NUV luminosity to derive the SFR. SFR and stellar masses are estimated with a Chabrier IMF. The MS is given in the following stellar mass and redshift ranges: $10^{8.5} - 10^{11.2}$ $M_\odot$ at $z \sim 0.6$, $z \sim 0.9$, $z \sim 1.1$ and $z \sim 1.4$, $10^{8.7} - 10^{11.2}$ $M_\odot$ at $z \sim 1.7$, $10^{9} - 10^{11.2}$ $M_\odot$ at $z \sim 2.25$ and $z \sim 2.75$, $10^{9.5} - 10^{11.5}$ $M_\odot$ at $z \sim 3.5$. We include in our analysis the stacked points at the observed stellar masses and redshift, as given in the paper.

• Santini et al. (2017) derive the MS in the ultra-deep Hubble Space Telescope Frontier fields. The MS is derived via SED fitting with a Salpeter IMF, BC03 SPS model and a Calzetti et al. (2000) extinction law. The MS location is derived via σ-clipping at the following stellar masses and redshift ranges: $10^{8} - 10^{10.6}$ $M_\odot$ at $1.3 < z < 2$, $10^{8} - 10^{11}$ $M_\odot$ at $2 < z < 3$ and $3 < z < 4$, $10^{8} - 10^{11}$ at $4 < z < 5$, and $10^{8.6} - 10^{11}$ $M_\odot$ at $5 < z < 6$. We estimate the MS by using the best fit relations in stellar mass bins of 0.25 dex to take into account stellar mass uncertainties.

• Kurczynski et al. (2016) utilize photometry in the Hubble Ultradeep Field (HUDF12) and Ultraviolet Ultra Deep Field (UVUDF) campaigns and CANDELS/GOODS-S to estimate the SFR via SED fitting. They use a Salpeter IMF, BC03 SPS model and a Calzetti et al. (2000) extinction law. The MS is identified via σ-clipping between 10^{7} and 10^{11} $M_\odot$ in the following redshift ranges: 0.5 – 1.0, 1.0 – 1.5, 1.5 – 2.0, 2.0 – 2.5 and 2.5 – 3.0. We point out that beyond $z \sim 1.5$, the stellar mass range $10^{10.2} - 10^{11}$ is populated by less than 20-25 systems. Thus, we limit the use of the MS estimates to the $10^{7} - 10^{10.2}$ $M_\odot$ stellar mass range. We estimate the MS by using the best fit relations in stellar mass bins of 0.25 dex to take into account stellar mass uncertainties.

• Pearson et al. (2018) use the SED modelling and fitting tool CIGALE to generate flux density priors in the Herschel SPIRE bands in the COSMOS field. These priors are fed into a deblending tool, called *XID+*, to extract flux densities from the SPIRE maps. As a last step, multi-wavelength data are combined with the extracted SPIRE flux densities to constrain SEDs and provide stellar masses and SFRs. These are used to populate the SFR-M^* plane over the redshift range $0.2 < z < 6$. The SED fitting is performed with a Chabrier IMF, BC03 SPS model, and a Charlot & Fall (2000) extinction law. Star forming galaxies are selected through the UVJ selection as in Whitaker et al. (2014). The MS is estimated in the

following stellar mass and redshift ranges: between 10^9 and 10^{11} $M_\odot$ at $0.2 < z < 0.5$ and $0.5 < z < 0.8$, between $10^{9.5}$ and 10^{11} $M_\odot$ at $0.8 < z < 1.1$, $1.1 < z < 1.4$ and $1.4 < z < 1.8$, between 10^{10} and 10^{11} $M_\odot$ at $1.8 < z < 2.3$ and $2.3 < z < 2.9$, between $10^{10,5}$ and 10^{11} $M_\odot$ at $2.9 < z < 3.9$ and $3.9 < z < 4.9$ and above 10^{11} $M_\odot$ at $4.9 < z < 6$. We estimate the MS by using the best fit relations in stellar mass bins of 0.25 dex to take into account stellar mass uncertainties.

- Belfiore et al. (2018) provide a measure of the local MS at $z < 0.05$ in the MaNGA sample (Bundy et al. 2015). Star forming galaxies are selected as those classified as star foming according to the BPT diagram in any spaxel of the MaNGA map. The SFR is estimated through the integrated, extinction corrected Hα emission over the galaxy region, converted via Robert C Kennicutt (1998) law and with a Chabrier IMF . The MS is estimated as the mean SFR in bins of stellar masses in the range $10^9 - 10^{11.5}$ $M_\odot$. We include in our analysis the mean points at the observed stellar masses and redshift.
- Davidzon et al. (2018) estimate the evolution of the specicic star formation rate at a fixed mass of $10^{10.3}$ $M_\odot$. The SFR is derived by the evolution of the galaxy stellar mass function of active galaxies of Davidzon et al. (2017), under the assumption that the stellar mass growth of a galaxy is mainly driven the integral of the SFR history, minus the quantity of stellar mass returned to the interstellar medium. The GSMF of active galaxies, and thus, the derived SFR evolution is based on the (M_{NUV}-M_R) − (M_R-M_J) colors. The SED fitting technique used in this analysis is based on a Chiabrier IMF. The MS is estimated at $z \sim 2.22$, 2.75, 2.25, 3.75, 5, 6 and 7.
- Lee et al. (2018) use the deep CANDELS observations in the GOODS North and South fields to revisit the correlations between stellar mass and star formation rate in galaxies at $1.2 < z < 4$. The quantities are estimated via SED fitting with a Chabrier IMF and a BC03 SPS model. SFGs are selected through the UVJ selection. The MS is estimated at stellar masses above 10^9 $M_\odot$ and in the following redshift bins: 1.2 − 1.5, 1.5 − 2, 2 − 2.8 and 2.8 − 4.
- Popesso et al. (2019b) provide measures of the local MS at $z < 0.085$ and stellar masses $> 10^{10}$ $M_\odot$ based on several SFR indicators. These include SDSS dust corrected Hα emission (Brinchmann et al. 2004), WISE 22 μm emission, dust corrected UV emission (Salim et al. 2016) and *Herschel* PACS and SPIRE emission at 100, 160, 250, 350 and 500 μm (Valiante et al. 2016). We include all of them in the analysis. The SFR are all based on a Chabrier IMF. The MS is estimated as the peak of the SFR distribution in several stellar mass bins in the SFR-stellar mass plane. We include in our analysis the mean points at the observed stellar masses and redshift.
- Popesso et al. (2019a) measure the evolution of the MS up to z~2.5 in the stellar mass range $10^{10} - 10^{11.5}$ $M_\odot$. The SFR is derived by a combination of IR fluxes based on *Spitzer* MIPS 24 μm and *Herschel* PACS and SPIRE data and NUV emission available in the CANDELS and COSMOS fields. The SFR and stellar masses are based on a Chabrier IMF. The MS is estimated as the peak of the SFR distribution in several stellar mass and redshift bins at $0.3 < z < 0.5$, $0.5 < z < 0.8$, $0.8 < z < 1.2$, $1.2 < z < 1.6$, $1.6 < z < 2.2$ and $2.2 < z < 2.5$. This corresponds to the median SFR in a log-normal distribution.
- Leslie et al. (2020) measure the evolution of the MS in the COSMOS field by exploting the VLA-COSMOS 3 GHz Large Project dataset. The MS is estimated in the range $0.3 < z < 6$ in the stellar mass range $10^9 - 10^{11}$ $M_\odot$ with different completeness limits as a function of the redshift. The median SFR is estimated via stacking in radio data in several redshift and stellar mass bins. We consider here only the bins where the prior galaxy sample is complete in stellar mass, as indicated by the authors. The SFR is estimated with a Chabrier IMF and following the KE12 calibration for radio emission. SFGs are selected as in Ilbert et al. (2013) through the NUVRJ color-color selection.

This paper has been typeset from a TEX/LATEX file prepared by the author.